

# Four $\text{Ca}^{2+}$ Ions Activate TRPM2 Channels by Binding in Deep Crevices near the Pore but Intracellularly of the Gate

László Csanády and Beáta Törőcsik

Department of Medical Biochemistry, Semmelweis University, Budapest, H-1094, Hungary

TRPM2 is a tetrameric  $\text{Ca}^{2+}$ -permeable channel involved in immunocyte respiratory burst and in postischemic neuronal death. In whole cells, TRPM2 activity requires intracellular ADP ribose (ADPR) and intra- or extracellular  $\text{Ca}^{2+}$ , but the mechanism and the binding sites for  $\text{Ca}^{2+}$  activation remain unknown. Here we study TRPM2 gating in inside-out patches while directly controlling intracellular ligand concentrations. Concentration jump experiments at various voltages and  $\text{Ca}^{2+}$  dependence of steady-state single-channel gating kinetics provide unprecedented insight into the molecular mechanism of  $\text{Ca}^{2+}$  activation. In patches excised from *Xenopus laevis* oocytes expressing human TRPM2, coapplication of intracellular ADPR and  $\text{Ca}^{2+}$  activated  $\sim 50$ -pS nonselective cation channels;  $K_{1/2}$  for ADPR was  $\sim 1$   $\mu\text{M}$  at saturating  $\text{Ca}^{2+}$ . Intracellular  $\text{Ca}^{2+}$  dependence of TRPM2 steady-state opening and closing rates (at saturating [ADPR] and low extracellular  $\text{Ca}^{2+}$ ) reveals that  $\text{Ca}^{2+}$  activation is a consequence of tighter binding of  $\text{Ca}^{2+}$  in the open rather than in the closed channel conformation. Four  $\text{Ca}^{2+}$  ions activate TRPM2 with a Monod-Wyman-Changeux mechanism: each binding event increases the open-closed equilibrium constant  $\sim 33$ -fold, producing altogether  $10^6$ -fold activation. Experiments in the presence of 1 mM of free  $\text{Ca}^{2+}$  on the extracellular side clearly show that closed channels do not sense extracellular  $\text{Ca}^{2+}$ , but once channels have opened  $\text{Ca}^{2+}$  entering passively through the pore slows channel closure by keeping the “activating sites” saturated, despite rapid continuous  $\text{Ca}^{2+}$ -free wash of the intracellular channel surface. This effect of extracellular  $\text{Ca}^{2+}$  on gating is gradually lost at progressively depolarized membrane potentials, where the driving force for  $\text{Ca}^{2+}$  influx is diminished. Thus, the activating sites lie intracellularly from the gate, but in a shielded crevice near the pore entrance. Our results suggest that in intact cells that contain micromolar ADPR a single brief puff of  $\text{Ca}^{2+}$  likely triggers prolonged, self-sustained TRPM2 activity.

## INTRODUCTION

TRPM2 belongs to the melastatin-related subfamily of transient receptor potential proteins (Nagamine et al., 1998) and forms a cation-selective ion channel, which is permeable to  $\text{Na}^+$ ,  $\text{K}^+$ , and  $\text{Ca}^{2+}$  (Perraud et al., 2001; Sano et al., 2001). It is abundantly expressed in the brain and in immune cells of the monocytic lineage and is activated under conditions of oxidative stress. TRPM2 activity plays important roles in the respiratory burst of neutrophil granulocytes and macrophages and in delayed neuronal cell death after ischemic stroke (for review see Nilius et al., 2007).

The TRPM2 protein is 1,503 amino acids long (Nagamine et al., 1998) and forms homotetrameric channels (Maruyama et al., 2007). In addition to the canonical TRPM family sequences, TRPM2 contains a 270-amino acid C-terminal NUDT9-H domain homologous to the ubiquitous mitochondrial NUDT9 enzyme that hydrolyzes ADP ribose (ADPR) into AMP and ribose-5-phosphate (Perraud et al., 2001). TRPM2 channel currents are activated by intracellular ADPR and the isolated NUDT9-H domain is an active ADPR hydrolase (Perraud et al., 2001, 2003). Many other adenine nucleotides

have been implicated in channel regulation (Kolisek et al., 2005; Beck et al., 2006; Grubisha et al., 2006); and oxidative stress induced by hydrogen peroxide ( $\text{H}_2\text{O}_2$ ) also leads to TRPM2 activation in intact, TRPM2-expressing cells, although it is still a matter of debate whether  $\text{H}_2\text{O}_2$  acts directly on TRPM2 or by perturbing adenine nucleotide metabolism (Wehage et al., 2002; Perraud et al., 2005; Buelow et al., 2008).

Early work has shown that activation of TRPM2 by ADPR is strongly potentiated by  $\text{Ca}^{2+}$  (Perraud et al., 2001). Biochemical studies have shown that calmodulin (CAM) binds to the TRPM2 protein; thus, CAM might be involved in the  $\text{Ca}^{2+}$  regulation of channel activity (Tong et al., 2006). Both intra- and extracellular  $\text{Ca}^{2+}$  enhance TRPM2 currents in whole-cell patch-clamp experiments, but intracellular  $\text{Ca}^{2+}$  plays a more prominent role (McHugh et al., 2003). A recent extensive study on  $\text{Ca}^{2+}$  dependence of TRPM2 whole-cell currents has led to the postulation of an extracellular  $\text{Ca}^{2+}$ -binding site on the channel that is involved in its activation when intracellular  $\text{Ca}^{2+}$  concentration ( $[\text{Ca}^{2+}]_i$ ) is low

Correspondence to László Csanády: laszlo.csanady@eok.sote.hu

Abbreviations used in this paper: ADPR, ADP ribose; CAM, calmodulin, cRNA, complementary RNA; MWC, Monod-Wyman-Changeux.

© 2009 Csanády and Törőcsik. This article is distributed under the terms of an Attribution-Noncommercial-Share Alike-No Mirror Sites license for the first six months after the publication date (see <http://www.jgp.org/misc/terms.shtml>). After six months it is available under a Creative Commons License (Attribution-Noncommercial-Share Alike 3.0 Unported license, as described at <http://creativecommons.org/licenses/by-nc-sa/3.0/>).

(Starkus et al., 2007). The mechanism by which  $\text{Ca}^{2+}$  regulates TRPM2 activity is not understood.

A caveat to the interpretation of most TRPM2-related studies to date is the limited suitability of the whole-cell patch-clamp technique (Hamill et al., 1981) for studying the biophysics of gating of a channel primarily affected by ligands from the intracellular side. In such studies each experiment is limited to the use of a single composition of intracellular (pipette) solution that gradually dialyzes the cell interior. First, because the rate of current development is limited by the slow time course of this diffusional equilibration (which occurs over tens of seconds), such experiments provide no information on the kinetics of single-channel gating, thus precluding dissection of molecular mechanisms. Second, to construct a dose-response curve, each ligand concentration is tested in a different cell, while channel expression varies from cell to cell. Third, the assumption that the cytosolic face of TRPM2 channels experiences a solution identical to the pipette solution is not necessarily true, given that the majority of the cellular machinery is still in place, including enzymes that produce or metabolize ADPR, compartments that can rapidly take up or release  $\text{Ca}^{2+}$ , as well as plasma membrane pumps, and channels that may alter submembrane  $[\text{Ca}^{2+}]$  despite strong exogenous buffering. Thus, because of the complexity of the entire cell it is hard to distinguish direct effects on TRPM2 itself from indirect effects that alter some intracellular factor involved in the regulation of the channel.

To study TRPM2 gating more directly, and at a single-molecule resolution, we have established a system for expressing TRPM2 in *Xenopus laevis* oocytes and for selective recording of TRPM2 currents in excised inside-out patches in which the concentrations of ligands bathing the cytosolic surface of the channels can be directly and rapidly controlled. With combined analysis of steady-state, single-channel recordings and macroscopic concentration jump experiments at various voltages we have elucidated the mechanism of  $\text{Ca}^{2+}$  activation and the spatial location of the binding sites for activating  $\text{Ca}^{2+}$  ions on the TRPM2 channel. Our results firmly establish that these “activating sites” are found intracellularly of the gate, but not on the protein surface. Rather, they are buried in a shielded vestibule in immediate vicinity of the mouth of the pore. The affinity for  $\text{Ca}^{2+}$  is higher in the open channel state, and binding of four  $\text{Ca}^{2+}$  ions results in an overall  $\sim 10^6$ -fold activation that is well described by the Monod-Wyman-Changeux (MWC) model. Our findings bear important implications for our understanding of how TRPM2 channels respond to metabolic signals in intact cells.

## MATERIALS AND METHODS

### Molecular Biology

The full-length human TRPM2 cDNA clone, inserted into pCMV6-XL4, was purchased from OriGene Technologies, Inc. The 5.6-kb

insert was excised using EcoRI and XbaI and subcloned into the corresponding sites of pGEMHE (Liman et al., 1992). The resulting hTRPM2/pGEMHE construct was confirmed by automated sequencing. For in vitro transcription, plasmid DNA was linearized by NheI; complementary RNA (cRNA) was prepared using a T7 mMessage mMachine kit (Applied Biosystems) and quantified on denaturing gels.

### Isolation and Injection of *Xenopus* Oocytes

*Xenopus* oocytes were isolated and injected with cRNA as previously described (Chan et al., 2000). Oocytes were defolliculated by collagenase treatment in a  $\text{Ca}^{2+}$ -free Ringer's solution and stored at 18°C in Ringer's supplemented with 1.8 mM  $\text{CaCl}_2$  and 50  $\mu\text{g}/\text{ml}$  gentamycin. To obtain various levels of channel expression, 0.1–10 ng of hTRPM2 cRNA was injected in a constant 50-nl volume and recordings were done 2–3 d after injection.

### Calibration of $\text{Ca}^{2+}$ Concentrations

To determine free  $[\text{Ca}^{2+}]$  in the micromolar range, we used Ca-Green 5N (Invitrogen) fluorescence (excitation, 505 nm; emission, 535 nm). Apparent binding parameters of this dye at 25°C and pH 7.1 were obtained by stepwise titration with  $\text{CaCl}_2$  (Fig. S1, available at <http://www.jgp.org/cgi/content/full/jgp.200810109/DC1>). Using these parameters we then measured a free  $[\text{Ca}^{2+}]$  of 4.4  $\mu\text{M}$  in our 140-mM sodium gluconate-based bath solution in the absence of high-affinity chelators and without added  $\text{Ca}^{2+}$ . Careful two-way titrations revealed a  $K_d$  for calcium gluconate of  $\sim 20$  mM (Fig. S2) at 25°C and pH 7.1. Based on this  $K_d$ , a fraction  $\sim 1/8$  of total added  $\text{Ca}^{2+}$  is expected to remain free in 140 mM sodium gluconate. Further fluorescent measurements largely confirmed this prediction and verified that free  $[\text{Ca}^{2+}]$  was not affected by the addition of 32  $\mu\text{M}$  ADPR (Table S1).

Solutions with free  $[\text{Ca}^{2+}]$  of 8 nM, 30 nM, 100 nM, 300 nM, and 1  $\mu\text{M}$  were prepared based on calculations using Winmaxc and the resulting free  $[\text{Ca}^{2+}]$  was then verified using FURA-2 (Fig. S3 and Table S2).

### Excised-Patch Recordings

Patch pipettes were pulled from borosilicate glass and had resistances of 3–4 M $\Omega$  in our pipette solution. The tip of the pipette was filled up to  $\sim 1$ -cm height with a solution containing 140 mM sodium gluconate, 2 mM magnesium gluconate<sub>2</sub>, and 10 mM HEPES, pH 7.4, with NaOH; for experiments in 1 mM of extracellular  $\text{Ca}^{2+}$  we added 8 mM calcium gluconate<sub>2</sub>. The back of the pipette, containing the electrode, was filled with a solution containing 140 mM NaCl, 2 mM  $\text{MgCl}_2$ , and 10 mM HEPES, pH 7.4, with NaOH. The bath solution (140 mM sodium gluconate, 2 mM magnesium gluconate<sub>2</sub>, and 10 mM HEPES, pH 7.1, with NaOH) was supplemented with 0  $\mu\text{M}$ , 32  $\mu\text{M}$ , 100  $\mu\text{M}$ , 320  $\mu\text{M}$ , 1 mM, or 3.2 mM calcium gluconate<sub>2</sub> to obtain 4.4, 7.6, 14.8, 43.6, 125, and 398  $\mu\text{M}$  free  $[\text{Ca}^{2+}]$ , respectively. To obtain 8 nM, 30 nM, 100 nM, 300 nM, and 1  $\mu\text{M}$  free  $[\text{Ca}^{2+}]$ , we added 1 mM EGTA and 0, 70, 240, 500, and 760  $\mu\text{M}$  Ca (gluconate)<sub>2</sub>, respectively, and readjusted the pH to 7.1.  $\text{Na}_2\text{ADPR}$  (Sigma-Aldrich) was added from a 32-mM aqueous stock solution. Patches were excised and transferred into a custom-made micromanifold accommodating eight flow lines, connected to the bath electrode through a 140-mM KCl-agar bridge, where the cytoplasmic surface was continuously superfused at 25°C with standard bath solution containing various test substances. This flow chamber had a dead volume of  $\sim 8$   $\mu\text{l}$  and the flow rate of the bath solution was  $\sim 0.5$  ml/min. Switching between solutions was implemented by computer-driven electric valves (HEKA) and occurred with minimal mixing; the kinetics of solution exchange was characterized by a delay of  $\sim 1$  s (because of the dead volume), followed by an abrupt transition period. To measure solution exchange rate, endogenous  $\text{Ca}^{2+}$ -activated  $\text{Cl}^-$  channel currents were activated by application of 1 mM of intracellular

$\text{Ca}^{2+}$  in the presence of a NaCl-based intracellular solution, and the rate of decay of this  $\text{Cl}^-$  current upon rapid removal of intracellular  $\text{Cl}^-$  (Fig. 1 A) was fitted by a single exponential, yielding an estimate of  $58 \pm 10 \text{ s}^{-1}$  ( $n = 16$ ) for the rate of solution exchange. Membrane currents were recorded at  $25^\circ\text{C}$ , filtered at 2 kHz, digitized at 10 kHz, and saved to disk using an Axopatch-200B amplifier, a Digidata 1322A board, and pCLAMP 9 software (MDS Analytical Technologies).

### Single-Channel Conductances

Unitary current amplitudes ( $i$ ) were determined by fitting multiple Gaussian functions to all-points histograms. Plots of  $i$  versus membrane voltage were fitted by linear regression to obtain slope conductances.

### Non-stationary Noise Analysis of Macroscopic Channel Currents

Open probability ( $P_o$ ) can be estimated from stationary noise analysis of macroscopic currents (Sakmann and Neher, 1995). Assuming identical and independent channels and using binomial theory, the mean  $m(I)$  and variance  $\sigma^2(I)$  of the macroscopic current ( $I$ ) can be expressed from  $P_o$  as  $m(I) = N iP_o$  and  $\sigma^2(I) = N i^2 P_o(1 - P_o)$ , respectively ( $N$  is the number of active channels and  $i$  is the unitary current size). From these equations it follows that  $\sigma^2(I)/i = (1 - P_o)m(I)$ . Thus, for a stationary segment of re-

cord the ratio between  $\sigma^2(I)/i$  and  $m(I)$  yields an estimate of  $1 - P_o$  (i.e., of  $P_o$ ). To sample the full variance of the macroscopic current caused by single-channel gating fluctuations, a stationary segment must be long compared with the mean time (the cycle time) required for a single channel to visit all possible single-channel states; segments that are too short underestimate the variance.

To estimate the  $P_o$  of TRPM2 channels during the time course of rundown (Fig. 1 B and Fig. 2 A), we adapted the above approach to make it applicable to situations where quasi-stationary current segments of sufficient length cannot be obtained. Because in longer segments the current declines by a sizeable fraction, the variance of such a segment is the sum of the variance caused by single-channel gating fluctuations and that of the monotonous current drift. To isolate the variance of the gating fluctuations, we first fitted the decaying current  $I$  (Fig. 2 A, black trace) with a single exponential (Fig. 2 A, red line), and then subtracted this fit line from the current trace to obtain the time course of gating noise ( $\hat{I}$ ) devoid of macroscopic drifts (Fig. 2 A, blue trace). We then split the experimental time course into segments of length  $\tau \ln(5/3)$ , where  $\tau$  is the time constant of the fitted exponential. Within such a segment the current falls to  $\sim 60\%$  of its initial value, i.e., at its two ends it differs by approximately  $\pm 20\%$  from its mean. Finally, for each obtained segment of time (Fig. 2 A, colored bars) we plotted  $-\sigma^2(\hat{I})/i$  as a function of  $-m(I)$  (Fig. 2 B, colored circles).

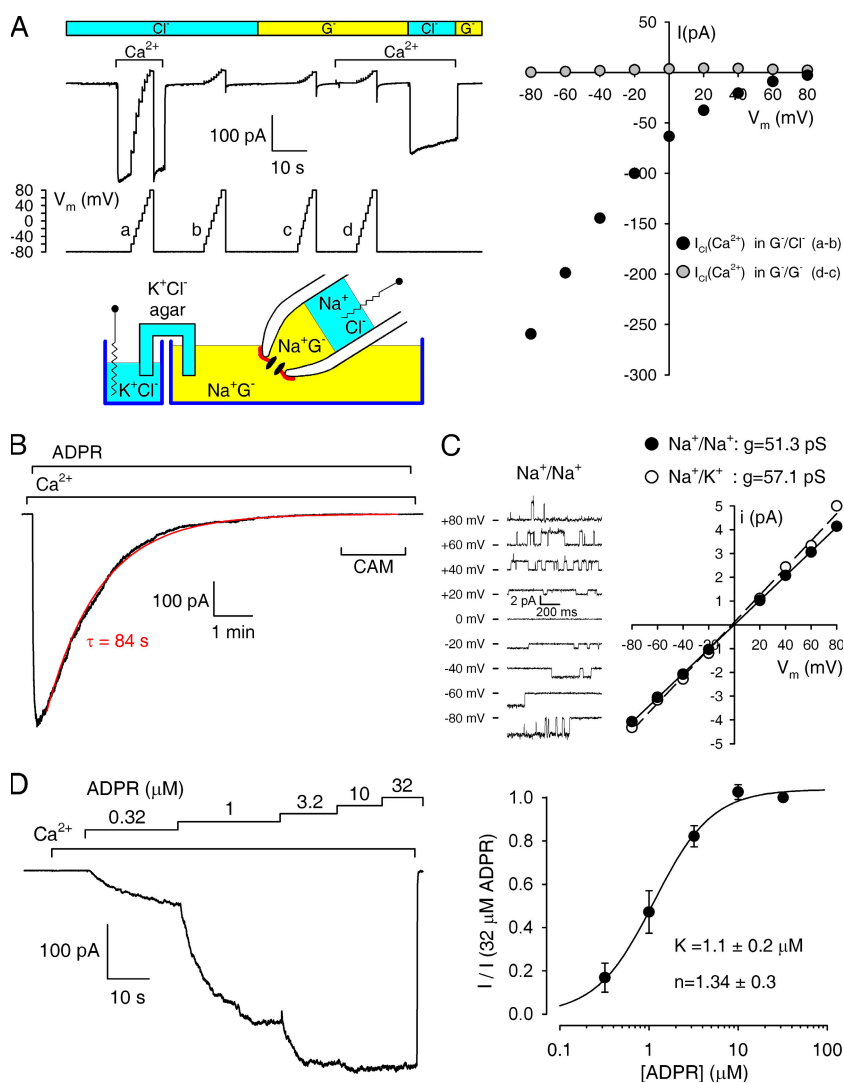


**Figure 1.** Basic properties of human TRPM2 channels expressed in *Xenopus* oocytes. (A, left) Cartoon (bottom) illustrates conditions to eliminate endogenous  $\text{Ca}^{2+}$ -activated  $\text{Cl}^-$  currents (top). Steady-state membrane currents in an inside-out patch from a noninjected oocyte, elicited by sequences of voltage steps between  $-80$  and  $+80$  mV (a–d), were assayed in the absence (b and c) and presence (a and d) of bath  $\text{Ca}^{2+}$  with gluconate ( $\text{G}^-$ ) as the main anion in the pipette but  $\text{Cl}^-$  (a and b) or  $\text{G}^-$  (c and d) alternating (colored bar) in the bath. (right)  $\text{Ca}^{2+}$ -activated currents as a function of voltage for the  $\text{G}^-/\text{Cl}^-$  (black circles) and  $\text{G}^-/\text{G}^-$  (gray circles) conditions. Bath-free  $[\text{Ca}^{2+}]$  was  $125 \mu\text{M}$  during test a and  $1 \text{ mM}$  during test d;  $K_{1/2}$  for the  $\text{Ca}^{2+}$ -activated  $\text{Cl}^-$  current is  $<4 \mu\text{M}$  (Kuruma and Hartzell, 2000). (B) Macroscopic TRPM2 current at  $-20$  mV, evoked by exposure to  $125 \mu\text{M}$   $\text{Ca}^{2+}$  +  $32 \mu\text{M}$  ADPR of a patch from an oocyte injected with  $10 \text{ ng}$  hTRPM2 cRNA. Red line is a single-exponential fit; CAM,  $200 \text{ nM}$  bovine CAM. (C, left) Unitary currents in symmetrical  $140 \text{ mM}$   $\text{Na}^+$ . (right) Single-channel current voltage relationships extracted from the traces to the left (closed circles) and from another patch in  $\text{Na}^+/\text{K}^+$  (open circles), both fitted by straight lines to obtain slope conductances. (D, left) Macroscopic TRPM2 current at  $-20$  mV elicited by rapid sequential exposure to increasing [ADPR] (bar) in the presence of  $125 \mu\text{M}$   $\text{Ca}^{2+}$ . (right) Currents at test [ADPR], normalized to that elicited in the same patch by  $32 \mu\text{M}$  ADPR, were plotted as a function of [ADPR] and fitted to the Hill equation (solid line). Data are represented as mean  $\pm$  SEM. Pipette  $[\text{Ca}^{2+}]$  was  $\sim 4 \mu\text{M}$  in all panels.



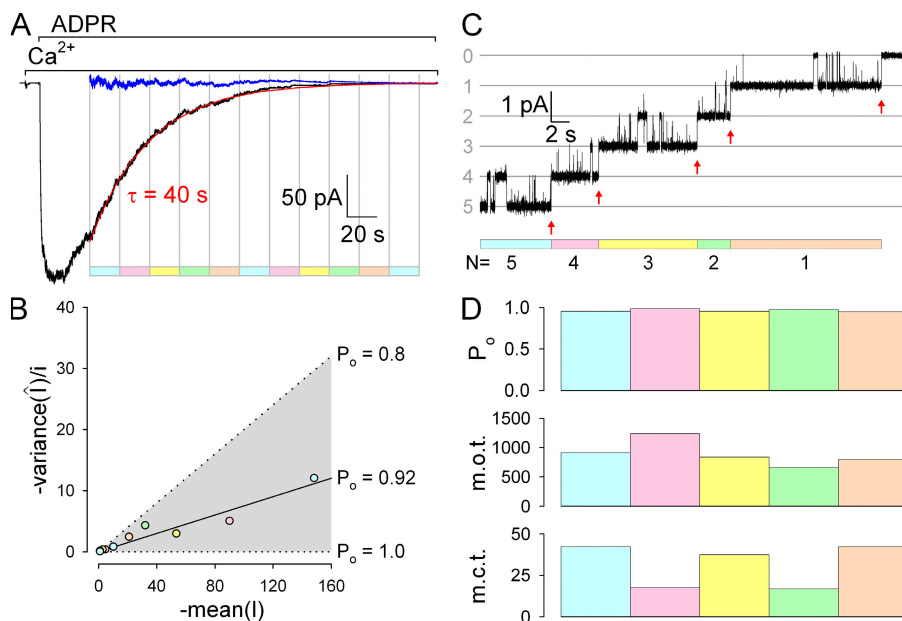


**Figure 2.** The rundown of TRPM2 currents in excised patches reflects a progressive decline in the number of active channels. (A) Macroscopic TRPM2 current ( $I$ ; black trace) activated in an inside-out patch by exposure to 32  $\mu\text{M}$  ADPR and 125  $\mu\text{M}$   $\text{Ca}^{2+}$  (bars). Red line is a single-exponential fit to the time course of current rundown, which was subtracted from the current trace to obtain the time course of gating noise ( $\hat{I}$ ; blue trace). Vertical gray lines and colored bars identify consecutive time windows over which the mean of  $I$  and the variance of  $\hat{I}$  were calculated. (B) Plot of  $-\sigma^2(\hat{I})/i$  as a function of  $-\text{mean}(I)$  (colored circles), calculated for the segments of time shown in A. The solid black line was obtained by linear regression through the data and corresponds to a  $P_o$  of 0.93. Gray shaded area identifies the region corresponding to  $P_o$  values  $>0.8$ . (C) Current from five TRPM2 channels recorded in the

continuous presence of 398  $\mu\text{M}$   $\text{Ca}^{2+}$  plus 32  $\mu\text{M}$  ADPR. Red arrows mark the time points of irreversible inactivation of the individual channels. Colored bars identify time windows with constant  $N$  (between two red arrows). (D) Stability plots of  $P_o$ , mean open time (m.o.t.), and mean closed time (m.c.t.) for the five individual time windows with constant  $N$ , identified by color coding in C. Values were obtained by the cycle-time method (see section 4 in the online supplemental material, available at <http://www.jgp.org/cgi/content/full/jgp.200810109/DC1>) and are not corrected for missed events because of the filter dead time. Pipette  $[\text{Ca}^{2+}]$  was  $\sim 4$   $\mu\text{M}$  in both A and C.

We tested the new method extensively on simulated records (Fig. S4, available at <http://www.jgp.org/cgi/content/full/jgp.200810109/DC1>) and found that it was suitable to (a) discriminate between high, intermediate, and low  $P_o$  values and (b) discern a constant number of channels gating with a gradually declining  $P_o$  from a progressively declining number of channels gating at constant  $P_o$ . In particular, for a declining  $N$  with constant  $P_o$ , the variance/mean plots produce straight lines (Fig. S4, A–C), whereas in the case of a declining  $P_o$  these plots are characteristically curved, producing increasing slope values as the current approaches zero (Fig. S4 D).

#### Kinetic Analysis of Patches with Small Numbers of Channels

Currents from segments of record with no more than 10 superimposed channel openings were baseline subtracted, Gaussian filtered at 200 Hz, and idealized by half-amplitude threshold crossing using a 1-ms fixed dead time (Csanády, 2000).  $P_o$  was calculated from the resulting events lists using the cycle-time method:  $P_o = (\sum_k l_k t_k) / (NT)$ , where  $l_k$  and  $t_k$  are the conductance level and duration of the  $k$ th event,  $N$  is the total number of active channels, and  $T = \sum_k t_k$ . Although we only studied mean opening ( $k_{CO}$ ) and closing rates ( $k_{OC}$ ), defined as the inverses of the mean closed and open times, respectively, we extracted these using a method that includes a correction for the dead time (unlike the cycle-time method). At all  $\text{Ca}^{2+}$  concentrations, single-channel gating showed clear bursting behavior; brief closures of  $\sim 2$ -ms duration interrupted bursts of openings flanked by longer, interburst closures. Thus, we chose the  $C_1$ – $C_2$ – $O_3$  scheme to simultaneously fit the dwell-time histograms of all conductance levels by maximum likelihood (Csanády, 2000), obtaining rate estimates  $r_{12}$ ,  $r_{21}$ ,  $r_{23}$ , and  $r_{32}$ . Mean opening and closing rates were then calculated as  $k_{CO} = r_{23} [r_{12} / (r_{12} + r_{21})]$  and  $k_{OC} = r_{32}$  (Colquhoun and Sigworth, 1995).

For low micromolar  $[\text{Ca}^{2+}]_i$  we mostly used patches in which  $N$  (estimated from bracketing segments at 125  $\mu\text{M}$   $\text{Ca}^{2+}$ ) was  $>10$ . Such segments were first fitted assuming a channel number  $N' = 10$ ,

which returns an unbiased estimate for  $k_{OC}$  but overestimates  $k_{CO}$ . The correct opening rate was then obtained from the two simple relationships  $N'P_o' = NP_o$  (where  $P_o'$  is the open probability obtained by the cycle-time method assuming  $N'$  channels) and  $P_o = k_{CO} / (k_{CO} + k_{OC})$ . Thus,  $k_{CO} = k_{OC}NP_o' / (N - NP_o')$ .

For  $[\text{Ca}^{2+}]_i > 40$   $\mu\text{M}$ ,  $P_o$  approached unity, and we only studied segments of record with no more than 10 active channels. Because segments with constant  $N$  were short due to the rundown, we generalized the method described in Csanády (2000) to an ensemble maximum likelihood fitting of many such short records, using for each segment its own individual  $N$  value (the maximum current level in that segment), but a single common value for the four fitted rate constants (Fig. S5, available at <http://www.jgp.org/cgi/content/full/jgp.200810109/DC1>). Thus, to extract opening and closing rates at 43.6, 125, and 398  $\mu\text{M}$   $[\text{Ca}^{2+}]_i$  and low extracellular  $\text{Ca}^{2+}$  (see Fig. 5, B and C, closed circles) ensembles of 5, 12, and 18 segments were fitted, respectively; whereas 6, 16, and 16 segments, respectively, were fitted to obtain the corresponding parameters at 1 mM of extracellular  $\text{Ca}^{2+}$  (see Fig. 5, B and C, open circles).

#### Model Fitting

Fitting TRPM2 gating by the MWC model is a simplification: the 10 states depicted in Fig. 5 D are compound states and the rates printed on the arrows represent mean steady-state rates of transition among these. A clear indication of such further complexity is that even at saturating  $[\text{Ca}^{2+}]_i$ , which should restrict channel gating to the two rightmost states in Fig. 5 D (all black), the distribution of closed event durations contains at least two exponential components. However, the principle of microscopic reversibility also applies to such compound systems regarding ligand concentration dependence of mean opening and closing rates (Csanády and Adam-Vizi, 2004), allowing us to use the MWC model to fit  $[\text{Ca}^{2+}]_i$  dependence of these simple mean parameters.

The MWC model for a channel with  $n$   $\text{Ca}^{2+}$ -binding sites predicts  $[\text{Ca}^{2+}]$  dependence of opening rate, closing rate, and  $P_o$  in the following forms:

$$k_{\text{CO}} = \alpha \left[ \frac{K_{\text{dc}} + g[\text{Ca}^{2+}]}{K_{\text{dc}} + [\text{Ca}^{2+}]} \right]^n,$$

$$k_{\text{OC}} = \beta \left[ \frac{K_{\text{do}} + f[\text{Ca}^{2+}]}{K_{\text{do}} + [\text{Ca}^{2+}]} \right]^n,$$

$$\text{and } P_o = \frac{k_{\text{CO}}}{k_{\text{CO}} + k_{\text{OC}}}$$

(Monod et al., 1965; see Fig. 5 D for notation). The ensemble of the three dose-response curves for  $P_o$ ,  $k_{\text{CO}}$ , and  $k_{\text{OC}}$  (Fig. 5, A–C, closed circles), obtained as described in the previous section, were fitted to the above three equations by minimizing the sum of the squared errors for all the data points in the three plots with respect to the five free parameters  $\alpha$ ,  $\beta$ ,  $f$ ,  $g$ , and  $K_{\text{dc}}$  ( $K_{\text{do}} = (f/g)K_{\text{dc}}$ ). Increasing  $n$  values yielded increasingly better fits, but the improvement became negligible for  $n > 4$  (Fig. S6, available at <http://www.jgp.org/cgi/content/full/jgp.200810109/DC1>).

#### Online Supplemental Material

Section 1 of the online supplemental material describes equations used for calibration of Ca-Green 5N fluorescence (illustrated by Fig. S1) and for determination of the  $K_d$  of calcium gluconate (illustrated by Fig. S2); Table S1 summarizes measured free  $[\text{Ca}^{2+}]$  in our sodium gluconate-based bath solutions without added EGTA. Section 2 describes equations used for calibration of FURA-2 fluorescence (illustrated by Fig. S3); Table S2 summarizes measured free  $[\text{Ca}^{2+}]$  in our sodium gluconate-based bath solutions containing 1 mM EGTA. Section 3 summarizes testing of our noise analysis algorithm on simulated datasets using four different gating models (illustrated by Fig. S4). Section 4 describes equations used for ensemble maximum likelihood fitting of a large number of short segments of record (illustrated by Fig. S5) and compares the efficiency of this procedure for estimation of rate constants from simulated records containing missed events to that of the cycle-time method. Section 5 shows global fits by the MWC model to the data in Fig. 5 assuming  $n$  values ranging from 1 to 10 (Fig. S6). Online supplemental material is available at <http://www.jgp.org/cgi/content/full/jgp.200810109/DC1>.

## RESULTS

### Human TRPM2 is Efficiently Expressed in *Xenopus* Oocytes and Forms Cation Channels Activated by ADPR and $\text{Ca}^{2+}$

*Xenopus* oocytes have been successfully used for expression and characterization of many ion channels including TRPM8 (Rohacs et al., 2005), a homologue of TRPM2, and were selected for this study. Because TRPM2 requires intracellular  $\text{Ca}^{2+}$  for activation and *Xenopus* oocytes exhibit large  $\text{Ca}^{2+}$ -activated  $\text{Cl}^-$  currents, we replaced  $\text{Cl}^-$  on both sides of the membrane with gluconate, a bulky anion that does not permeate through endogenous  $\text{Ca}^{2+}$ -activated  $\text{Cl}^-$  channels (Qu and Hartzell, 2000). Patch pipettes were half filled with a sodium gluconate-based

solution and a NaCl-based saline was carefully layered on top to secure a high  $[\text{Cl}^-]$  for the pipette electrode (Fig. 1 A, left). After patch excision, the tip of the patch pipette was placed into a fast perfusion device with continuous flow, connected to the bath electrode via a KCl-agar bridge. This allowed addition/removal of bath chloride without affecting electrode potentials. With  $\text{Cl}^-$  in the bath, addition of  $\text{Ca}^{2+}$  to the cytosolic face of patches excised from noninjected oocytes induced large inward currents (Fig. 1 A, left, test a vs. b) which did not reverse (Fig. 1 A, right, black circles), as expected for a  $\text{Cl}^-$ -selective current. In contrast, in symmetrical sodium gluconate, addition of cytosolic  $\text{Ca}^{2+}$  failed to induce any endogenous currents (Fig. 1 A, left, test d vs. c, and Fig. 1 A, right, gray circles). We therefore chose to study TRPM2 channels in symmetrical sodium gluconate at a membrane potential of  $-20$  mV (unless otherwise indicated).

In patches excised from oocytes injected with 10 ng of human TRPM2 cRNA, cytosolic exposure to ADPR plus  $\text{Ca}^{2+}$  instantaneously elicited large TRPM2 currents, which then started to decay in the maintained presence of both activating ligands (Fig. 1 B). This slow “rundown,” already reported for both human (Sano et al., 2001) and rat TRPM2 (Hill et al., 2006) expressed in mammalian cells, had a time constant of 1–2 min and was neither prevented nor reversed by application of 200 nM CAM (Fig. 1 B), application of 25  $\mu\text{M}$  dioctanoyl phosphatidylinositol 4,5-bisphosphate (not depicted), application of 300 nM of catalytic subunit of protein kinase A + 1 mM ATP (not depicted), or lowering of intracellular  $[\text{Mg}^{2+}]$  to 200  $\mu\text{M}$  (not depicted).

TRPM2 unitary currents, assayed in patches from oocytes injected with smaller amounts (0.1–1 ng) of cRNA, were linear and reversed at near zero millivolts in both symmetrical  $\text{Na}^+$  (Fig. 1 C, traces and closed circles) or with  $\text{Na}^+$  in the pipette and  $\text{K}^+$  in the bath (Fig. 1 C, open circles). Single-channel slope conductances were  $51.3 \pm 1.6$  pS ( $n = 6$ ) and  $57.1 \pm 0.8$  pS ( $n = 5$ ), respectively, under these two conditions, similar to those reported before for TRPM2 expressed in mammalian cells (Perraud et al., 2001; Sano et al., 2001).

We next determined the apparent affinity of macroscopic TRPM2 currents for ADPR by superfusing the cytosolic face of macroscopic patches with increasing  $[\text{ADPR}]$  in saturating  $[\text{Ca}^{2+}]_i$ . Applications of various test  $[\text{ADPR}]$  were either bracketed by applications of maximal (32  $\mu\text{M}$ )  $[\text{ADPR}]$  or executed in a rapid sequence (Fig. 1 D, left) to avoid distortion by rundown. Normalized currents were plotted against  $[\text{ADPR}]$  (Fig. 1 D, right) and fitted with the Hill equation (solid line). To our surprise, TRPM2 channels were activated by ADPR with a  $K_{1/2}$  of  $1.1 \pm 0.2$   $\mu\text{M}$ , contrasting at least an order of magnitude higher  $K_{1/2}$  values obtained in previous whole-cell studies (Perraud et al., 2001; Sano et al., 2001; Kolisek et al., 2005). Note that 125  $\mu\text{M}$   $\text{Ca}^{2+}$  alone failed to elicit TRPM2 currents, nor was 32  $\mu\text{M}$  ADPR sufficient

to maintain TRPM2 activity after  $\text{Ca}^{2+}$  removal (Fig. 1 D, left). Thus,  $\text{Ca}^{2+}$  and ADPR are both required for TRPM2 activation, which is consistent with an earlier report (McHugh et al., 2003).

Together, these experiments confirm that human TRPM2 is efficiently expressed in *Xenopus* oocytes yielding channels with properties very similar to those seen in mammalian expression systems.

#### The Rundown in Excised Patches Reflects Progressive, Irreversible Inactivation, rather than a Graded Decline in Channel Open Probability

Before attempting to study the kinetics of gating of single TRPM2 channels we first had to address the kinetic nature of the rundown. To obtain an estimate of  $P_o$  without any assumptions about the number of channels, we subjected the rundown time courses of macroscopic TRPM2 currents in the presence of saturating [ADPR] and  $[\text{Ca}^{2+}]_i$  (Fig. 2 A) to noise analysis (see Materials and Methods and Fig. S4). To this end, current decay time courses ( $I$ ; Fig. 2 A, black trace) were fitted by single exponentials (Fig. 2 A, red line), and the time course of pure gating noise ( $\hat{I}$ ; Fig. 2 A, blue trace) was isolated by subtracting the fit line from the current. The variance of  $\hat{I}$  and the mean of  $I$  were calculated for consecutive time segments (Fig. 2 A, colored bars), and  $-\sigma^2(\hat{I})/i$  was plotted as a function of  $-m(I)$  (Fig. 2 B, colored circles). In all cases tested, these plots were reasonably linear and had small slopes.  $P_o$  values obtained by linear regression through all the points in such plots (Fig. 2 B, black line) were high ( $P_o = 0.92 \pm 0.01$  [ $n = 5$ ]), and the majority of the data points fell into the area of the graphs corresponding to  $P_o$  values  $>0.8$  (Fig. 2 B, gray shaded area). These data indicate that the rundown in excised patches, observed in the presence of saturating [ADPR] and  $[\text{Ca}^{2+}]_i$ , reflects progressive, irreversible inactivation of channels gating with high  $P_o$ , rather than a graded decline in channel open probability.

A closer observation of patches with smaller numbers of channels (Fig. 2 C) exposed to saturating ligand con-

centrations ( $>40 \mu\text{M}$   $[\text{Ca}^{2+}]_i$  and  $32 \mu\text{M}$  ADPR) confirmed that the rundown indeed consisted of a progressive irreversible loss of active channels over time (Fig. 2 C, red arrows), while the remaining channels continued to gate with a high  $P_o$  approaching unity (also see Fig. 4 A, right, expanded segments on bottom). Splitting such records into brief segments in which  $N$  could be considered constant (i.e., between two red arrows in Fig. 2 C;  $N$  was taken as the maximum number of simultaneously open channels) allowed us to construct stability plots of mean closed time, mean open time, and  $P_o$  (Fig. 2 D, each bar corresponds to the short segment of time identified in Fig. 2 C by color coding). Such plots did not reveal any strong tendencies in the gating parameters of the surviving channels; the large stochastic variations in mean open and closed times seen in Fig. 2 D rather reflect the small numbers of gating events in each individual segment with constant  $N$ . Thus, neither  $P_o$  nor the kinetics of gating of individual surviving channels is drastically affected by the rundown.

#### Micromolar Intracellular $\text{Ca}^{2+}$ Is Required for TRPM2 Activation at Saturating [ADPR]

We next determined the apparent affinity of TRPM2 currents for activation by intracellular  $\text{Ca}^{2+}$  in the presence of saturating ( $32 \mu\text{M}$ ) ADPR. With nominally zero ( $\sim 4 \mu\text{M}$ )  $\text{Ca}^{2+}$  in the pipette solution, we exposed macroscopic inside-out patches to various test  $[\text{Ca}^{2+}]_i$ , bracketed by exposures to our control  $[\text{Ca}^{2+}]_i$  of  $125 \mu\text{M}$  (Fig. 3 A). Fractional currents at each test  $[\text{Ca}^{2+}]_i$ , obtained by normalization to the mean current observed in bracketing  $125\text{-}\mu\text{M}$  segments, were plotted as a function of  $[\text{Ca}^{2+}]_i$  (Fig. 3 B, closed circles) and fitted to the Hill equation (solid line) to yield a  $K_{1/2}$  of  $22.4 \pm 0.9 \mu\text{M}$  and a Hill coefficient  $n = 1.62 \pm 0.08$  (Fig. 3 B). This low apparent affinity and Hill coefficient for TRPM2 activation by  $\text{Ca}^{2+}$  in excised patches contrasts an  $\sim 50$ -fold smaller  $K_{1/2}$  and  $n$  of  $\sim 5$  estimated in previous whole-cell studies (McHugh et al., 2003; Starkus et al., 2007). Of note, we could detect only slight changes in

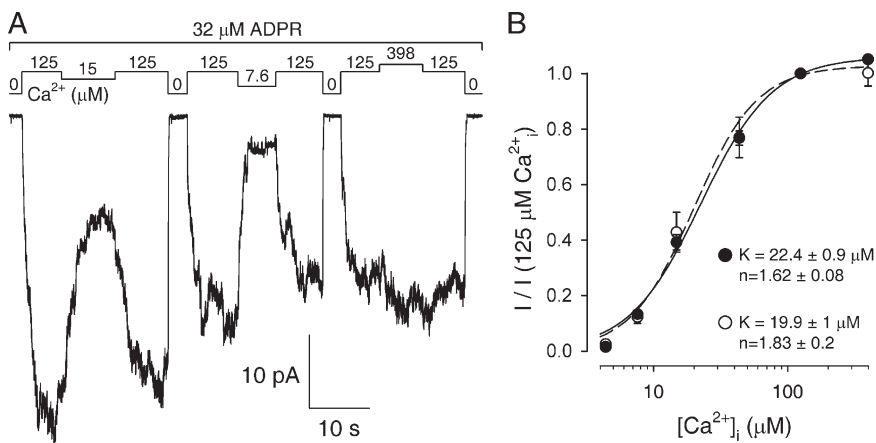


**Figure 3.** Activation of macroscopic TRPM2 currents requires micromolar  $[\text{Ca}^{2+}]_i$ . (A) Macroscopic TRPM2 current from an inside-out patch superfused with  $32 \mu\text{M}$  ADPR and various test  $[\text{Ca}^{2+}]_i$ , bracketed by exposures to  $125 \mu\text{M}$   $\text{Ca}^{2+}$  (bars). Pipette  $[\text{Ca}^{2+}]$  was  $\sim 4 \mu\text{M}$ . (B) Mean currents in test  $[\text{Ca}^{2+}]_i$ , normalized to the mean of the currents in bracketing  $125\text{-}\mu\text{M}$   $\text{Ca}^{2+}$  segments, were plotted against  $[\text{Ca}^{2+}]_i$  and fitted to the Hill equation. Pipette  $[\text{Ca}^{2+}]$  was either  $\sim 4 \mu\text{M}$  (closed circles and solid fit line) or  $1 \text{ mM}$  (open circles and dashed fit line). Data are represented as mean  $\pm$  SEM.

the apparent affinity for  $\text{Ca}^{2+}$  over the time course of an experiment.

#### $\text{Ca}^{2+}$ Dependence of Opening and Closing Rates Reveals MWC Type Activation Mechanism

To obtain information about mechanism, we investigated  $[\text{Ca}^{2+}]_i$  dependence of single-channel gating kinetics at saturating  $[\text{ADPR}]$  (Fig. 4 A), while maintaining extracellular (pipette)  $[\text{Ca}^{2+}]$  at nominally zero ( $\sim 4 \mu\text{M}$ ). This was a nontrivial task. First, in the face of the continuous rundown the slow gating of TRPM2 channels hampers collection of sufficient gating events at steady state (see Fig. 2 D). We therefore analyzed patches with multiple channels in which individual gating events were still well resolved (Fig. 4 A, see expanded traces on bottom) but more events could be recorded over shorter time periods. Second, the pattern of single-channel gating is complex, containing at least two populations of closed events. We therefore limited our analysis to extracting, for each  $[\text{Ca}^{2+}]_i$ , mean opening and closing rates, defined as the inverses of the mean closed and open times, respectively. These parameters can be conveniently extracted from multichannel patches, provided that the number of active channels ( $N$ ) is known (Fig. 4 A and Materials and methods).

Thus, for  $>40 \mu\text{M}$   $[\text{Ca}^{2+}]_i$  we obtained opening and closing rates from a global fit (see Materials and methods) to a large ensemble of short segments of record in each of which  $N$  could be considered constant (i.e., between

two red arrows in Fig. 4 A, right). In contrast, the low  $P_o$  activity at low micromolar  $[\text{Ca}^{2+}]_i$  was analyzed in patches with larger numbers of channels (Fig. 4 A, left current trace), and  $N$  in such test segments was estimated by linear interpolation between the  $N$  values determined for bracketing segments at saturating  $[\text{Ca}^{2+}]$ .

A plot of open probabilities obtained in this fashion yielded a dose-response curve (Fig. 5 A, closed circles) in good agreement with the  $\text{Ca}^{2+}$  dependence of macroscopic TRPM2 current (Fig. 3 B, closed circles). Activation of  $P_o$  by intracellular  $\text{Ca}^{2+}$  reflected a large stimulation of channel opening rate (Fig. 5 B, closed circles), whereas closing rates (Fig. 5 C, closed circles) remained at  $\sim 1 \text{ s}^{-1}$  and were little influenced by  $[\text{Ca}^{2+}]_i$  in the micromolar range (see the expanded current traces in Fig. 4 A).

If channel closing rate were truly independent of  $[\text{Ca}^{2+}]_i$ , then the rate of decay of macroscopic current should reflect this constant closing rate under circumstances in which the opening rate is zero, e.g., upon sudden removal of intracellular  $\text{Ca}^{2+}$ . Intriguingly, we invariably observed an  $\sim 20$  times faster macroscopic current decay upon  $\text{Ca}^{2+}$  removal (Fig. 1 D, Fig. 2 A, and Fig. 4 A), suggesting that the closing rate might also be affected by  $\text{Ca}^{2+}$ , but with an apparent affinity too high for its detection in steady-state records because channels cease to open at submicromolar  $[\text{Ca}^{2+}]_i$ .

To measure closing rate at such submicromolar  $[\text{Ca}^{2+}]_i$ , we resorted to macroscopic concentration jump experiments using a series of bath solutions in which free  $[\text{Ca}^{2+}]$

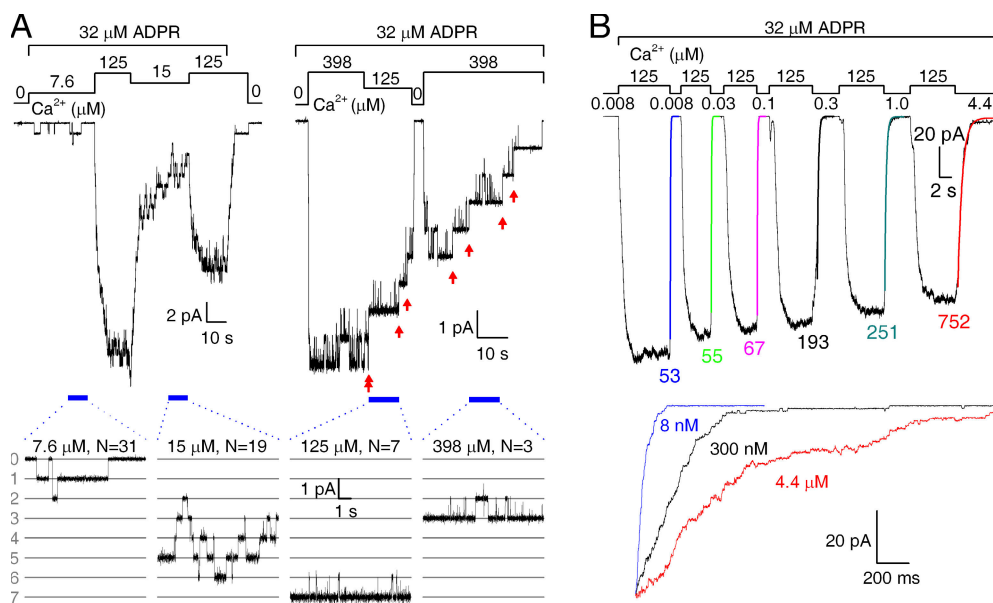


**Figure 4.** Determination of  $[\text{Ca}^{2+}]_i$  dependence of TRPM2 opening and closing rates. (A) Two representative current traces from patches with smaller numbers of TRPM2 channels superfused with various test  $[\text{Ca}^{2+}]_i$  (bars) in the presence of  $32 \mu\text{M}$  ADPR. Pipette  $[\text{Ca}^{2+}]$  was  $\sim 4 \mu\text{M}$ . (left) The number of channels ( $N$ ) in test segments at low micromolar  $\text{Ca}^{2+}$  (blue bars; expanded below) was obtained by linear interpolation of  $N$  in bracketing segments at saturating  $\text{Ca}^{2+}$ . (right) Test segments for  $[\text{Ca}^{2+}]_i > 40 \mu\text{M}$  were defined as the time periods between two occurrences of irreversible channel closure (red arrows). Within such segments (blue bars; expanded below)

$P_o$  approached unity and  $N$  was given by the maximum current level. (B) Closing rate at various submicromolar  $[\text{Ca}^{2+}]_i$  was studied in a macropatch; in the presence of  $32 \mu\text{M}$  ADPR TRPM2 channels were alternately exposed to  $125 \mu\text{M}$   $\text{Ca}^{2+}$  and various submicromolar test  $[\text{Ca}^{2+}]$  (bars); pipette  $[\text{Ca}^{2+}]$  was  $\sim 4 \mu\text{M}$ . Current decay time courses in various test  $[\text{Ca}^{2+}]_i$  were fitted by single exponentials (colored smooth lines and time constants [in milliseconds]); those in  $8 \text{ nM}$  (blue),  $300 \text{ nM}$  (black), and  $4.4 \mu\text{M}$   $\text{Ca}^{2+}$  (red) are shown below at an expanded time scale. Note the complete lack of reopening events in  $8$  and  $300 \text{ nM}$   $\text{Ca}^{2+}$ ; in  $4.4 \mu\text{M}$   $\text{Ca}^{2+}$  opening rate is still far smaller than closing rate as witnessed by the small remaining steady-state current.



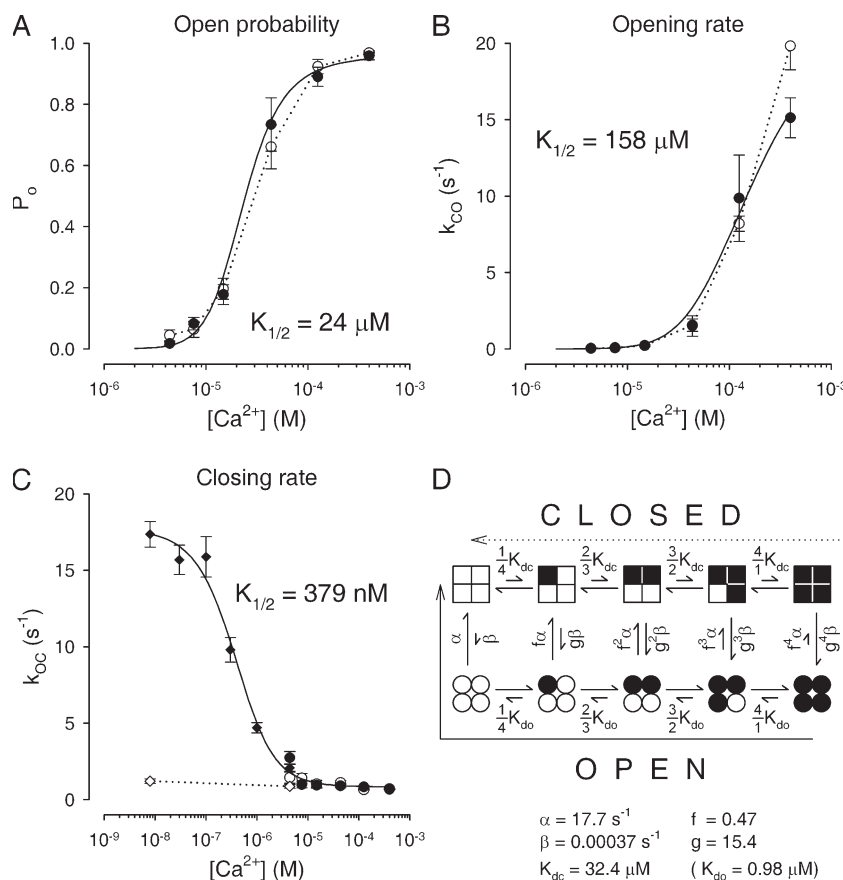


**Figure 5.**  $[Ca^{2+}]_i$  dependence of TRPM2 single-channel gating parameters is well described by the MWC model. (A–C) Steady-state (mean  $\pm$  SEM) open probabilities ( $P_o$ ; A), opening rates ( $k_{CO}$ ; B), and closing rates ( $k_{OC}$ ; C) of single TRPM2 channels at  $\geq 4.4 \mu M$   $Ca^{2+}$  are plotted (circles) as a function of  $[Ca^{2+}]_i$ . In C, diamonds represent closing rates at  $\leq 4.4 \mu M$   $Ca^{2+}$  determined from macroscopic current decay time courses. Pipette  $[Ca^{2+}]$  was either  $\sim 4 \mu M$  (closed circles) or  $1 mM$  (open circles and dotted lines). Solid black lines illustrate the fit of the data at low extracellular  $Ca^{2+}$  (closed circles) by the scheme in D. (D) MWC model with four  $Ca^{2+}$ -binding sites (1 site/subunit). Squares represent closed and circles represent open channel subunits; filled black symbols represent subunits with  $Ca^{2+}$  bound. Solid and dotted arrow indicate the pathways of channel closure upon rapid removal of intracellular  $Ca^{2+}$  in the absence and presence, respectively, of extracellular  $Ca^{2+}$ .

was buffered to 8 nM (our “zero- $Ca^{2+}$ ” solution), 30 nM, 100 nM, 300 nM, or 1  $\mu M$  using EGTA. We repeatedly activated macroscopic TRPM2 currents using 125  $\mu M$   $Ca^{2+}$ , followed by a sudden switch to these test  $Ca^{2+}$  levels (Fig. 4 B). The rate of current relaxation to a new equilibrium, elicited by a sudden change in the rates of gating, is given by the sum of the opening and the closing rate under the new condition. Because opening rates are extremely low at  $<5 \mu M$   $[Ca^{2+}]_i$ , the staircase-like current decay seen in these test segments (see expanded traces in Fig. 4 B, bottom) reflects channel closing rate, given by the inverse of the time constant of a fitted single exponential (Fig. 4 B, top, colored lines, time constants are in milliseconds). Our extended dose-response curve for channel closing rate (Fig. 5 C, closed diamonds) clearly showed a dose-dependent acceleration of channel closure by lowering  $[Ca^{2+}]_i$  in the sub-micromolar range. Importantly, for 4.4  $\mu M$   $[Ca^{2+}]_i$ , the concentration jump experiments yielded an estimate of closing rate similar to that obtained from steady-state single-channel analysis.

A simple mechanism by which a ligand can activate a channel is if the binding site has a higher affinity for the ligand in the open than in the closed channel conformation: by microscopic reversibility, ligand binding will then stabilize the open state. Because the apparent affinities for affecting opening and closing rate reflect the

ligand-binding affinity of the closed and open channel, respectively (Csanády and Adam-Vizi, 2004), the kinetic results in Fig. 5 (B and C) are compatible with such a mechanism. The fourfold symmetry of homotetrameric TRPM2 channels (Maruyama et al., 2007) implies at least four  $Ca^{2+}$ -binding sites, prompting us to consider the MWC model (Monod et al., 1965), a simple application of the aforementioned concept to a multimeric protein. In this model the channel retains its fourfold symmetry at all times (Fig. 5 D): the four subunits transit between open (circles) and closed (squares) conformations in a concerted manner. Ligand binding to individual subunits (Fig. 5 D, black symbols) are independent events and additively affect the energetics of the open-closed equilibrium by virtue of the difference in ligand dissociation constants of the open ( $K_{do}$ ) and the closed channel ( $K_{dc}$ ). In essence, each binding event alters the unliganded closing rate ( $\alpha$ ) and opening rate ( $\beta$ ) by some constant factor ( $f$  and  $g$ , respectively). We performed an ensemble fit (see Materials and methods) of the three dose-response curves for opening rate, closing rate, and  $P_o$  (Fig. 5, A–C, closed circles) using the model in Fig. 5 D and obtained an excellent fit to all three curves (Fig. 5, A–C, solid lines; predicted midpoints are plotted in each panel). Thus, in the presence of saturating ADPR, activation of TRPM2 by intracellular  $Ca^{2+}$  is well described by the MWC model with the kinetic parameters printed



in Fig. 5 D. The fact that the time courses of channel closure are reasonably fitted by single exponentials even in the 100-nM range (Fig. 4 B), where the population of open channels is likely distributed between several different open states (Fig. 5 D, bottom states), suggests that, at least for open channels,  $\text{Ca}^{2+}$  binding/unbinding is in rapid equilibrium compared with the rates of channel closure.

#### Closed Channels Do Not Sense Millimolar Extracellular $\text{Ca}^{2+}$

Because extracellular  $\text{Ca}^{2+}$  strongly potentiates TRPM2 whole-cell currents (McHugh et al., 2003; Starkus et al., 2007), we performed experiments similar to those in Figs. 2 and 4, but in the presence of 1 mM of free  $\text{Ca}^{2+}$  in the extracellular (pipette) solution. However, extracellular  $\text{Ca}^{2+}$  failed to affect fractional activation of macroscopic TRPM2 current by various  $[\text{Ca}^{2+}]_i$  in excised patches (Fig. 3 B, open circles), consistent with the findings of Starkus et al. (2007) in whole cells. Moreover, detailed analysis of steady-state single-channel gating parameters failed to detect any significant effect of extracellular  $\text{Ca}^{2+}$  on single-channel  $P_o$ , opening rates, or closing rates (Fig. 5, A–C, open circles).

Opening rate is a property of the closed channel and is strongly dependent on  $[\text{Ca}^{2+}]$  bathing the intracellular surface of the channels (Fig. 5 B, closed circles). Because the presence of 1 mM of extracellular  $\text{Ca}^{2+}$  does not affect this relationship (Fig. 5 B, open circles) we can conclude that under our experimental conditions, with the cytosolic face of the patch immersed into a rapidly flowing solution, the local  $[\text{Ca}^{2+}]$  experienced by the activating sites of a closed channel is not influenced by the absence or presence of extracellular  $\text{Ca}^{2+}$ . This strongly suggests that the activating sites are located on the intracellular side of the channel gate, where as soon as a channel closes, any local elevation in  $[\text{Ca}^{2+}]$ , caused by prior  $\text{Ca}^{2+}$  influx through the open pore, is instantaneously (within  $\sim 2 \mu\text{s}$ ; see Discussion) eliminated by the rapid vectorial flow of the bath solution.

#### Closure of Open Channels Is Slowed by Millimolar Extracellular $\text{Ca}^{2+}$

Closing rate is a property of the open channel but, in contrast to opening rate, TRPM2 closing rate is not sensitive to  $[\text{Ca}^{2+}]_i$  in the micromolar range (Fig. 5 C, closed circles). Therefore, the fact that 1 mM of extracellular  $\text{Ca}^{2+}$  failed to affect steady-state closing rates (Fig. 5 C, open circles) does not preclude the possibility that the presence of extracellular  $\text{Ca}^{2+}$  might elevate local  $[\text{Ca}^{2+}]$  around the activating sites of an open channel caused by  $\text{Ca}^{2+}$  ions entering through the pore. Such a possibility must be evaluated at some submicromolar  $[\text{Ca}^{2+}]_i$  at which channel closing rate is sensitive to  $[\text{Ca}^{2+}]$  (Fig. 5 C, closed diamonds).

We therefore examined the rate of decay of macroscopic TRPM2 current, activated by 32  $\mu\text{M}$  ADPR and saturating  $[\text{Ca}^{2+}]_i$ , upon sudden removal of intracellular  $\text{Ca}^{2+}$ , with 1 mM of free  $\text{Ca}^{2+}$  in the extracellular solution (Fig. 6 A). Again, like in the absence of extracellular  $\text{Ca}^{2+}$ , TRPM2 currents decayed as a staircase, with almost no channel opening events (Fig. 6 A, right trace and blue single-exponential fit line), but the time constant of channel closure was dramatically prolonged compared with that seen in the absence of extracellular  $\text{Ca}^{2+}$  (Fig. 6 A, left trace and red single-exponential fit line). On average, 1 mM of extracellular  $\text{Ca}^{2+}$  slowed channel closure in 8 nM  $[\text{Ca}^{2+}]_i$  by  $\sim 15$ – $20$ -fold (Fig. 6 A, inset) to the same level observed at steady state in micromolar  $[\text{Ca}^{2+}]_i$  (Fig. 5 C, compare open diamonds and circles).

Thus, even while the cytosolic surface of the channels is immersed into a rapidly flowing  $\text{Ca}^{2+}$ -free solution, the activating sites of an open TRPM2 channel experience a local  $[\text{Ca}^{2+}]$  in the micromolar range when  $\text{Ca}^{2+}$  is present on the extracellular side. This suggests that the activating sites are not on the protein surface but in a deep vestibule, in the immediate vicinity of the cytosolic mouth of the pore (Fig. 6 B). In the absence of extracellular  $\text{Ca}^{2+}$  (Fig. 6 B, top), sudden removal of intracellular  $\text{Ca}^{2+}$  results in immediate loss of  $\text{Ca}^{2+}$  from the activating sites, followed by channel closure at the fast rate ( $\sim 20 \text{ s}^{-1}$ ) characteristic of nonliganded channels (Fig. 5 D, pathway marked by solid arrow). In contrast, when  $\text{Ca}^{2+}$  is present on the extracellular side (Fig. 6 B, bottom),  $\text{Ca}^{2+}$  ions arrive through the pore as long as the gate is open and maintain a high local  $[\text{Ca}^{2+}]$  around the activating sites, keeping them saturated and allowing the channel to close at the slow rate of  $\sim 1 \text{ s}^{-1}$  characteristic of fully liganded channels (Fig. 5 D, pathway marked by dotted arrow). The fact that these channels, which must have closed in a fully liganded state (to top right state in Fig. 5 D), nevertheless do barely reopen (Fig. 6 A, right trace) indicates that in the absence of  $\text{Ca}^{2+}$  in the bath  $\text{Ca}^{2+}$  ions are lost from the activating sites much faster than the rate of reopening of a fully liganded channel (estimated  $\sim 20 \text{ s}^{-1}$ ; Fig. 5 B). This provides further support for the notion that  $\text{Ca}^{2+}$  binding/unbinding is a rapid equilibrium process compared with the rates of gating.

#### Slowing of Channel Closure by Extracellular $\text{Ca}^{2+}$ Is Prevented by Membrane Depolarization

If the slowing of channel closure by extracellular  $\text{Ca}^{2+}$  (Fig. 6 A) indeed requires entry of  $\text{Ca}^{2+}$  ions through the pore, then this effect should be dampened by conditions that decrease the electrochemical driving force for  $\text{Ca}^{2+}$  influx, e.g., by membrane depolarization. To test this idea, we studied the dependence on membrane potential of the delay in channel closure caused by extracellular  $\text{Ca}^{2+}$  (Fig. 7).

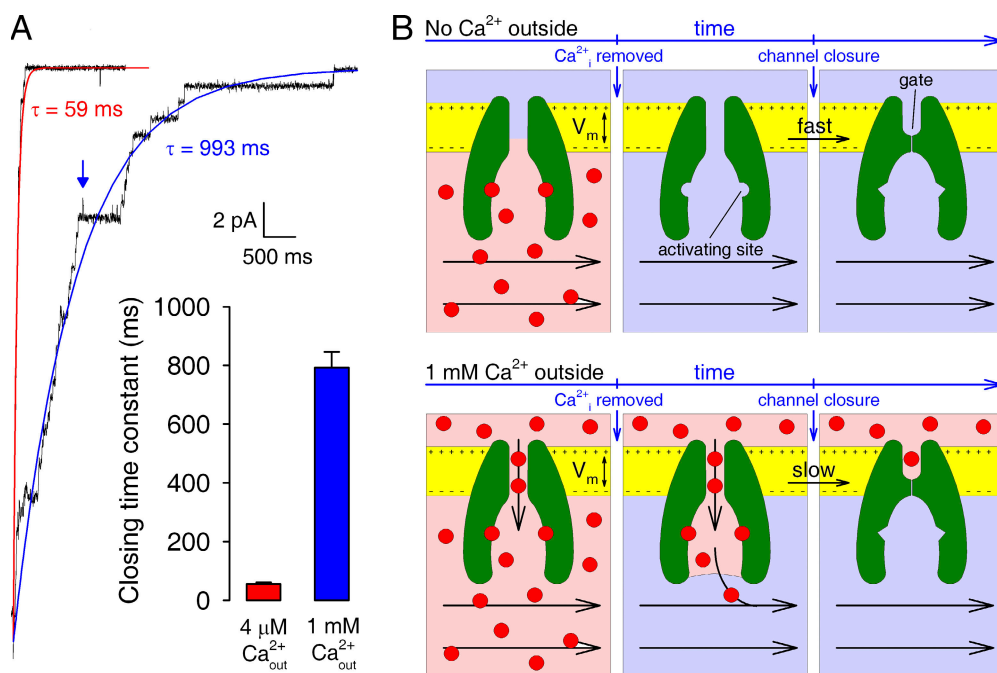


**Figure 6.** Closure of open channels is slowed by millimolar extracellular  $\text{Ca}^{2+}$ . (A) Representative time courses of macroscopic current decay upon sudden removal of intracellular  $\text{Ca}^{2+}$ , with  $\sim 4 \mu\text{M}$  (left trace) and  $1 \text{ mM}$  (right trace) free  $\text{Ca}^{2+}$  in the pipette solution. Smooth lines are single-exponential fits, with time constants shown. Inset shows mean  $\pm$  SEM decay time constants for the above two conditions. (B) Cartoon interpretation of channel closing kinetics when intracellular  $\text{Ca}^{2+}$  is washed away. (top) In the absence of extracellular  $\text{Ca}^{2+}$  the activating sites rapidly lose  $\text{Ca}^{2+}$  yielding unliganded channels that close fast (Fig. 5 D, solid arrow). (bottom) In the presence of extracellular  $\text{Ca}^{2+}$  the

activating sites, which are located in a deep vestibule near the pore entrance, remain liganded because of  $\text{Ca}^{2+}$  ions entering through the open pore. Thus, channels close at the slow rate characteristic of fully liganded channels (Fig. 5 D, dotted arrow). Once channels have closed, the activating sites, which are located intracellularly of the gate, are cut away from  $\text{Ca}^{2+}$ , hence channels remain shut. Note a few occasional reopening events in the right current trace in A, which typically follow brief closures (e.g., blue arrow), suggesting that some fraction of very brief closed events is too short to allow dissociation of  $\text{Ca}^{2+}$  from the activating sites. Such occasional reopenings might explain why in the presence of  $1 \text{ mM}$  of extracellular  $\text{Ca}^{2+}$  and  $4.4 \mu\text{M}$   $[\text{Ca}^{2+}]_i$  the macroscopic current relaxations yield a slightly smaller estimate of closing rate than the steady-state data (Fig. 5 C, white circle vs. diamond for  $4.4 \mu\text{M}$   $[\text{Ca}^{2+}]_i$ ).

Without added  $\text{Ca}^{2+}$  in the extracellular solution, in the presence of  $32 \mu\text{M}$  ADPR, similar sized currents (aside from slow continuous rundown) were evoked by brief pulses of  $125 \mu\text{M}$  of intracellular  $\text{Ca}^{2+}$  at identical absolute membrane potentials of opposing polarity (Fig. 7 A). More importantly, the rates of channel closure upon rapid removal of intracellular  $\text{Ca}^{2+}$  (i.e., upon lowering of  $[\text{Ca}^{2+}]_i$  to  $8 \text{ nM}$ ), obtained as the reciprocals of the time constants of fitted single exponentials (Fig. 7 A, colored solid lines [time constants are in milliseconds]), remained constant between voltages ranging from  $-80$  to  $+60 \text{ mV}$  (Fig. 7 C, black circles). These experiments show that under our experimental conditions TRPM2 channel gating possesses no significant intrinsic voltage dependence.

In contrast, with  $1 \text{ mM}$   $\text{Ca}^{2+}$  on the extracellular side channel closing rate in  $8 \text{ nM}$   $[\text{Ca}^{2+}]_i$  became strongly voltage dependent (Fig. 7 B). The slow decay time constant observed before at  $-20 \text{ mV}$  (Fig. 6 A) was further prolonged at more negative potentials, but became progressively shorter at depolarized potentials (Fig. 7 B, colored solid lines and time constants) approaching those seen in the absence of extracellular  $\text{Ca}^{2+}$  (Fig. 7 A). Between  $-80$  and  $+60 \text{ mV}$  depolarization accelerated closing rate by  $>10$ -fold (Fig. 7 C, red circles), consistent with the model in Fig. 6 B.

Because EGTA retains two protons at pH 7.1, titration of EGTA with  $\text{Ca}^{2+}$  results in  $\text{H}^+$  release. We therefore considered the possibility that  $\text{Ca}^{2+}$  ions entering through the pore might delay channel closure (Fig. 6 B) as a consequence of a local lowering of pH, rather than because of saturation of the activating sites. We repeated our experiments in Fig. 7 B using a zero  $\text{Ca}^{2+}$  bath solution made using  $1 \text{ mM}$  BAPTA (free  $[\text{Ca}^{2+}] \sim 7 \text{ nM}$ ). Because BAPTA is completely deprotonated at pH 7.1, a puff of  $\text{Ca}^{2+}$  ions into such a solution is not expected to affect local pH. We obtained identical results using either BAPTA or EGTA; the plots in Fig. 7 C contain data using both types of chelators.

**Apparent Affinity for Intracellular  $\text{Ca}^{2+}$  Is Little Sensitive to [ADPR] or to Replacement of Intracellular  $\text{Na}^+$  with  $\text{K}^+$**   
The apparent affinity for TRPM2 activation by  $\text{Ca}^{2+}$  we have measured in excised patches is  $>50$ -fold lower as compared with estimates in previous whole-cell studies (McHugh et al., 2003; Starkus et al., 2007), making us wonder what the reason for this discrepancy might be. Because in those studies much higher ADPR concentrations ( $0.5$  and  $1 \text{ mM}$ ) were used, we tested whether increasing [ADPR] to  $1 \text{ mM}$  might increase the apparent affinity for  $\text{Ca}^{2+}$  activation. However, the presence of  $1 \text{ mM}$  of intracellular ADPR failed to enhance fractional activation of macroscopic TRPM2 current by  $15 \mu\text{M}$  of

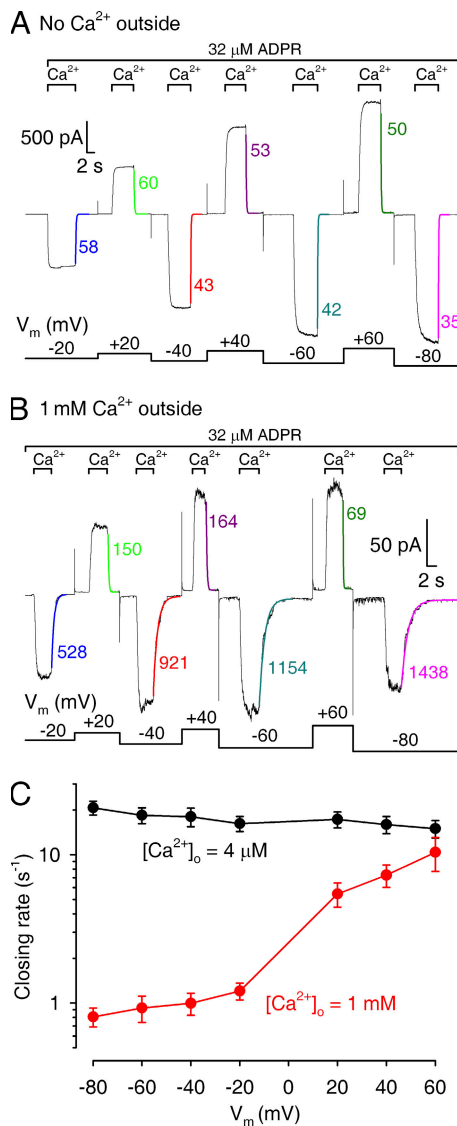


**Figure 7.** Depolarization removes the gating effect of extracellular  $\text{Ca}^{2+}$  by preventing  $\text{Ca}^{2+}$  influx through the open pore. (A and B) In the presence of 32  $\mu\text{M}$  ADPR macroscopic TRPM2 currents at various test potentials (bars below traces) were activated by exposure to 125  $\mu\text{M}$  of intracellular  $\text{Ca}^{2+}$  and closed by its sudden removal. Colored smooth lines are fitted single exponentials and time constants are in milliseconds. Pipette  $[\text{Ca}^{2+}]$  was  $\sim 4 \mu\text{M}$  in A and 1 mM in B. (C) Closing rates (mean  $\pm$  SEM) in zero  $[\text{Ca}^{2+}]_i$  and  $\sim 4 \mu\text{M}$  (black circles) or 1 mM (red circles) of free  $\text{Ca}^{2+}$  in the pipette solution, obtained as the reciprocals of current decay time constants (see A and B, respectively), are plotted against membrane potential.

intracellular  $\text{Ca}^{2+}$  ( $I_{15 \mu\text{M Ca}^{2+}}/I_{125 \mu\text{M Ca}^{2+}}$  was  $0.19 \pm 0.03$  [ $n = 5$ ]; compare to Fig. 3 B and Fig. 5 A).

Conversely, our  $K_{1/2}$  for TRPM2 activation by intracellular ADPR in the presence of saturating (125  $\mu\text{M}$ )  $[\text{Ca}^{2+}]_i$  (Fig. 1 D) was at least an order of magnitude smaller than previous whole-cell estimates (Perraud et al., 2001; Sano et al., 2001; Kolisek et al., 2005), which were obtained at lower intracellular  $[\text{Ca}^{2+}]$ . We therefore tested whether  $K_{1/2}$  for ADPR activation

would be increased at lower  $[\text{Ca}^{2+}]_i$ . However, lowering  $[\text{Ca}^{2+}]_i$  to  $\sim 15 \mu\text{M}$  did not significantly alter fractional activation by 1  $\mu\text{M}$  of intracellular ADPR, which remained about half-maximal ( $I_{1 \mu\text{M ADPR}}/I_{32 \mu\text{M ADPR}}$  was  $0.42 \pm 0.1$  [ $n = 7$ ]), with 10  $\mu\text{M}$  ADPR still saturating ( $I_{10 \mu\text{M ADPR}}/I_{32 \mu\text{M ADPR}}$  was  $1.1 \pm 0.3$  [ $n = 3$ ]; compare to Fig. 1 D). Thus, in excised patches the apparent affinities of TRPM2 for intracellular ADPR and intracellular  $\text{Ca}^{2+}$  are little sensitive to the concentration of the other ligand.

Under whole-cell conditions the sensitivity of TRPM2 current for various activating ligands was shown to be sensitive to the species of intracellular cation used (Beck et al., 2006; Starkus et al., 2007). We therefore tested whether replacing intracellular  $\text{Na}^+$  with the more physiological  $\text{K}^+$  might affect the apparent affinity for ADPR and/or  $\text{Ca}^{2+}$  activation of TRPM2 currents in excised patches. To this end we alternately exposed macroscopic patches to potassium gluconate-based bath solutions containing various test concentrations or 32  $\mu\text{M}$  ADPR, all in the presence of saturating  $[\text{Ca}^{2+}]_i$  (Fig. 8 A), and normalized the currents in various test  $[\text{ADPR}]$  to that obtained in the presence of 32  $\mu\text{M}$  ADPR in the same patch. A plot of normalized currents as a function of  $[\text{ADPR}]$  (Fig. 8 B, closed circles) resulted in a dose-response curve similar to that obtained with intracellular  $\text{Na}^+$  (Fig. 1 D); a fit to the Hill equation (Fig. 8 B, solid line) yielded  $K_{1/2} = 1.0 \pm 0.1 \mu\text{M}$  and  $n = 1.98 \pm 0.5$ .

Similarly, we exposed macroscopic patches to a potassium gluconate-based bath solution containing various test  $[\text{Ca}^{2+}]_i$ , bracketed by exposures to 125  $\mu\text{M}$   $[\text{Ca}^{2+}]_i$ , all in the presence of 32  $\mu\text{M}$  ADPR (Fig. 8 C; compare to Fig. 3 A). Plots of fractional current at various test  $[\text{Ca}^{2+}]_i$  yielded dose-response curves very similar to those seen in intracellular  $\text{Na}^+$  (Fig. 3 B), both when extracellular  $[\text{Ca}^{2+}]$  was 4  $\mu\text{M}$  ( $K_{1/2} = 31.9 \pm 3 \mu\text{M}$ ; Fig. 8 D, closed circles and solid fit line) or with 1 mM of free  $\text{Ca}^{2+}$  in the pipette solution ( $K_{1/2} = 22.8 \pm 2.8 \mu\text{M}$ ; Fig. 8 D, open circles and dotted fit line). Thus, in inside-out patches the apparent affinities for ADPR and  $\text{Ca}^{2+}$  activation of TRPM2 are little sensitive to whether  $\text{Na}^+$  or  $\text{K}^+$  is used as the intracellular cation.

## DISCUSSION

Since its cloning in 1998 (Nagamine et al., 1998), TRPM2 has been in the focus of intensive research, but the majority of these investigations were performed on intact cells, with limited control over the composition of the intracellular solution, and have provided little information on molecular mechanisms. The present study is the first in which TRPM2 channel gating has been scrutinized at the single-channel level in a cell-free system.

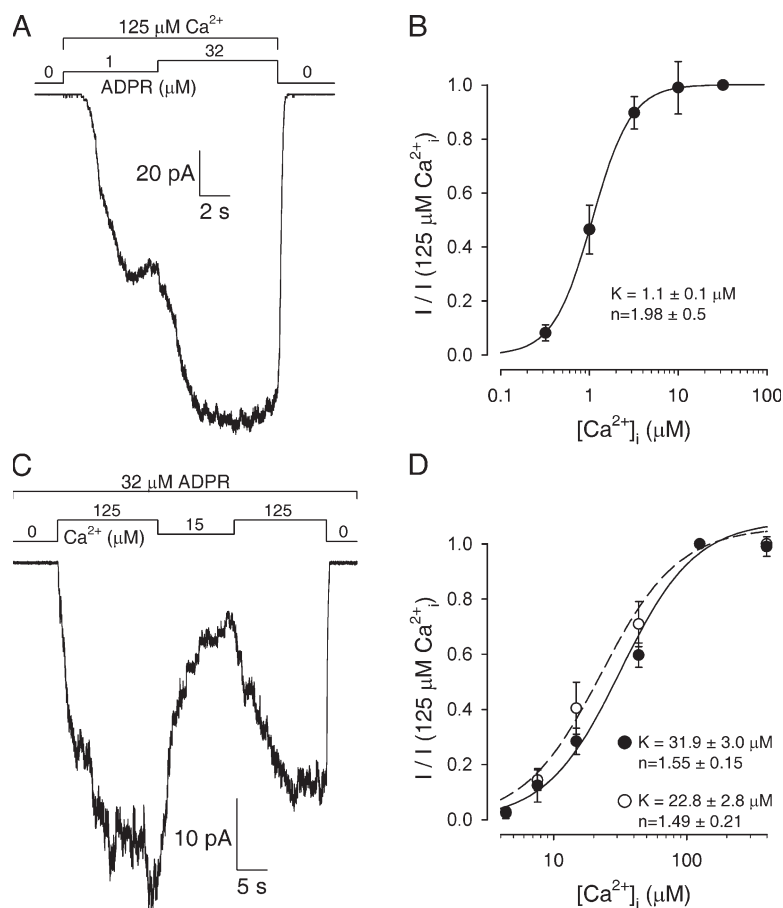


**Figure 8.** Apparent affinities for TRPM2 activation by intracellular  $\text{Ca}^{2+}$  and ADPR are not altered by replacing intracellular  $\text{Na}^+$  with  $\text{K}^+$ . (A) Macroscopic TRPM2 current elicited in an inside-out patch bathed in a potassium gluconate-based solution by rapid sequential exposure to 1 and 32  $\mu\text{M}$  [ADPR] (bar) in the presence of 125  $\mu\text{M}$   $\text{Ca}^{2+}$ . Pipette  $[\text{Ca}^{2+}]$  was  $\sim 4 \mu\text{M}$ . (B) Normalized dose-response curve for current activation by ADPR in potassium gluconate solution containing 125  $\mu\text{M}$  free  $\text{Ca}^{2+}$  (closed circles) and a fit by the Hill equation (solid line). (C) Macroscopic TRPM2 current from an inside-out patch superfused with potassium gluconate solution and 32  $\mu\text{M}$  ADPR; exposure to  $\sim 15 \mu\text{M}$   $[\text{Ca}^{2+}]_i$  was bracketed by exposures to 125  $\mu\text{M}$   $\text{Ca}^{2+}$  (bars). Pipette  $[\text{Ca}^{2+}]$  was  $\sim 4 \mu\text{M}$ . (D) Dose-response curve for activation by  $[\text{Ca}^{2+}]_i$  in potassium gluconate solution containing 32  $\mu\text{M}$  ADPR. Mean currents in test  $[\text{Ca}^{2+}]_i$ , normalized to the mean of the currents in bracketing 125- $\mu\text{M}$   $\text{Ca}^{2+}$  segments, were plotted against  $[\text{Ca}^{2+}]_i$  and fitted to the Hill equation. Pipette  $[\text{Ca}^{2+}]$  was either  $\sim 4 \mu\text{M}$  (closed circles and solid fit line) or 1 mM (open circles and dashed fit line). (B and D) Data are represented as mean  $\pm$  SEM.

The apparent affinities we have found for activation of TRPM2 by both  $\text{Ca}^{2+}$  and ADPR greatly differ from those established in whole-cell experiments (but see Lange et al., 2008). We have tested whether differences in our recording conditions could have affected channel activation, but have found that neither our lower [ADPR] nor the use of  $\text{Na}^+$  as the intracellular cation were responsible (Fig. 8). One possible explanation for the discrepancy could be a potential loss of some regulatory factor upon patch excision. However, a second possible explanation is that whole-cell TRPM2 currents do not saturate at  $\sim 1 \mu\text{M}$   $[\text{Ca}^{2+}]_i$ , similar to large-conductance  $\text{Ca}^{2+}$ -activated  $\text{K}^+$  channels that are activated in living cells by micromolar  $\text{Ca}^{2+}$  from sparks (Rothberg and Magleby, 1999; Pérez et al., 2001). This is because the effect of high micromolar intracellular  $\text{Ca}^{2+}$  on TRPM2 whole-cell currents has never been tested and so it cannot be excluded that further activation would have been obtained in such experiments. (Of note, our gating model [Fig. 5 D] also predicts an  $\sim 100$ -fold increase in  $P_o$  between  $[\text{Ca}^{2+}]_i$  values of 8 nM and 2  $\mu\text{M}$ , because of a decrease in channel closing rate; and the reliability of the “plateauing” seen at  $\sim 1 \mu\text{M}$   $\text{Ca}^{2+}$  in whole-cell dose-response curves is somewhat limited by the fact that in such experiments each individual ligand concentration is tested in a different cell.) An example supporting such a possibility is the

homologue TRPM4, for which a  $K_{1/2}$  value for  $\text{Ca}^{2+}$  activation of 320 nM was estimated from whole-cell current responses restricted to a range of  $[\text{Ca}^{2+}]_i$  between 100 nM and 1  $\mu\text{M}$  (Launay et al., 2002), whereas a  $K_{1/2}$  of 20  $\mu\text{M}$  was obtained for the same channel from whole-cell currents assayed over a range of  $[\text{Ca}^{2+}]_i$  between 100 nM and 100  $\mu\text{M}$  (Ullrich et al., 2005). Finally, it remains a possibility that in intact cells the local ligand concentrations that the channels experience might differ from the bulk cytosolic concentrations and that the concentration of one ligand influences the local concentration of the other, such that these remain poorly defined in whole-cell experiments. As an example, the almost all-or-none type activation by intracellular [ADPR] ( $n_H$  of  $\sim 9$ ) found in whole cells (Perraud et al., 2001) is at large with our findings in inside-out patches (Fig. 1 D) and, if taken at face value, would be hardly explained by any reasonable molecular mechanism. It seems more likely that, through the stimulation of TRPM2 open probability, increasing [ADPR] increasingly elevates local  $[\text{Ca}^{2+}]$  around the activating sites, yielding apparent positive feedback. Also along these lines, we found no evidence for voltage dependence of gating in symmetrical  $\text{Na}^+$ -based solutions, suggesting that such a phenomenon, reported in whole cells loaded with  $\text{Na}^+$  (Perraud et al., 2001; Fig. 7 A), was caused by voltage-dependent alteration of some cellular



parameter involved in TRPM2 regulation. Thus, although whole-cell studies have outlined TRPM2 as a channel regulated by a multitude of diverse factors in an extremely complex manner, further biophysical studies in cell-free patches will need to sort out which of those factors really act on the TRPM2 protein itself.

Consistent with previous observations (Sano et al., 2001; Hill et al., 2006), TRPM2 activity runs down in excised patches. Although all our efforts to prevent this rundown have so far failed, our detailed kinetic analysis (Fig. 2) revealed that the rundown consists of a progressive irreversible decline in the number of active channels, rather than of a graded decline in open probability. In the face of this technical challenge we have developed a significant collection of novel analytical tools to extract single-channel gating parameters using both noise analysis of macroscopic patches (Fig. 2 and Fig. S4) and ensemble maximum likelihood fitting of sets of dwell-time histograms (Fig. S5). These tools will prove useful for further studies of TRPM2 gating.

Through a combination of steady-state single-channel recordings and macroscopic concentration jump experiments we established  $[Ca^{2+}]_i$  dependence of single-channel gating parameters, including closing rates in the submicromolar  $[Ca^{2+}]$  range in which the channels do not open (Figs. 4 and 5). The MWC model, with four postulated  $Ca^{2+}$ -binding sites, provides an excellent framework for understanding the dependence of these parameters on  $[Ca^{2+}]_i$  in the presence of saturating ADPR. Although we cannot exclude the possibility of more than four  $Ca^{2+}$ -binding sites (Fig. S5), no more than four sites were required to fit the kinetic parameters of gating (Fig. 4). Our fit parameters suggest that binding of a single  $Ca^{2+}$  ion to an activating site, by virtue of its tighter binding in the open conformation, increases the open-closed equilibrium constant by a factor of  $\sim 33$  ( $g/f$ ; see Fig. 5 D), equivalent to an energetic stabilization of the open state by  $\sim 3.5$  kT or  $\sim 8.6$  kJ/mol.  $Ca^{2+}$  binding to all four sites activates TRPM2  $\sim 10^6$ -fold corresponding to a  $\sim 14$ -kT reduction of the open state free energy. As a comparison, the nicotinic acetylcholine receptor, the best studied ligand-gated channel, contains only two ligand-binding sites, and a comparable overall activation ( $\sim 10^8$ -fold) requires much larger effects ( $\sim 10^4$ -fold) of the two individual ligands (Jackson, 1986).

The rate of our solution exchange, estimated from the rate of decay of endogenous  $Ca^{2+}$ -activated  $Cl^-$  current upon sudden removal of  $Cl^-$  (Fig. 1 A) was  $\sim 50$  s $^{-1}$ , less than  $\sim 3$  times faster than the fastest TRPM2 closing rates we have measured ( $\sim 20$  s $^{-1}$ ; Fig. 5 C, closed diamonds). It is therefore likely that this maximal closing rate of unliganded TRPM2 is slightly underestimated. Steady-state analysis of the small number of openings we could collect from segments of record at 8 nM of intra-

cellular and  $\sim 4$   $\mu$ M of extracellular  $Ca^{2+}$ , from 14 patches with very large numbers of channels, gave an estimate for closing rate of  $27 \pm 5$  s $^{-1}$ . Nevertheless, this potential inaccuracy does not affect the conclusions of our study.

Our experiments have outlined the probable location of the  $Ca^{2+}$ -binding sites on the TRPM2 channel responsible for activation of gating. The clear demonstration that these binding sites sense extracellular  $Ca^{2+}$  when the pore is open, but not when the pore is closed (Figs. 5 and 6), allows us to assign them with great confidence to a location intracellularly of the gate. This conclusion is further corroborated by our demonstration that membrane depolarization, which slows the rate of  $Ca^{2+}$  entry through the open pore, reduces the effect of extracellular  $Ca^{2+}$  on the activating sites of an open channel (Fig. 7). In contrast, the dramatic slowing by external  $Ca^{2+}$  of channel closure upon removal of intracellular  $Ca^{2+}$  (Fig. 6 A) suggests that  $Ca^{2+}$  ions entering through the pore are able to keep the activating sites saturated as long as the pore remains open (Fig. 6 B, bottom). This is intriguing because, at a molecular level, the rate at which the cytosolic surface of the channels was superfused with  $Ca^{2+}$ -free solution can be designated at best as extreme. From the 18-nm diameter of the TRPM2 channel structure (Maruyama et al., 2007) and the  $\sim 1$ -cm/s flow rate of our bath solution we calculate that the entire solution volume in contact with the channel surface is continuously displaced by fresh  $Ca^{2+}$ -free solution every  $\sim 2$   $\mu$ s. Note that this rate of continuous rinsing is much faster than the rate of solution exchange, which reflects the rate of passage over the patch of a thin layer of solution of mixed composition (requiring  $\sim 20$  ms; see Materials and methods). We estimate that despite this extremely intensive  $Ca^{2+}$ -free surface wash the activating sites of an open channel experience high micromolar  $[Ca^{2+}]$  when extracellular  $Ca^{2+}$  is present and the membrane potential is negative (Fig. 5 C and Fig. 7C). These sites must therefore be buried in some deep crevice, shielded from the protein surface, near the intracellular mouth of the pore. The recent, low-resolution electron microscopic reconstruction of TRPM2 revealed a bell-shaped channel structure, consisting of a small compact half-dome pointing toward the extracellular side and a large, sparse intracellular domain containing multiple internal cavities (Maruyama et al., 2007). Based on our functional results we consider these cavities as the most likely candidates for the location of the  $Ca^{2+}$ -binding sites responsible for TRPM2 activation.

The broader significance of our dissection of the biophysical properties of single TRPM2 molecules is that these provide important clues for understanding the regulation of TRPM2 activity in intact cells. Although TRPM2 channels are believed to act as coincidence detectors of simultaneous rises in intracellular [ADPR] and  $[Ca^{2+}]$ , our results suggest that these two ligands

regulate TRPM2 with very different dynamics. In our inside-out patches exposed to a flowing  $\text{Ca}^{2+}$ -free solution activating  $\text{Ca}^{2+}$  ions were washed away as soon as a channel closed; hence extracellular  $\text{Ca}^{2+}$  alone was insufficient to maintain steady-state gating. In contrast, under the static conditions of an intact cell (even in the presence of strong exogenous  $\text{Ca}^{2+}$  buffering!) the local  $[\text{Ca}^{2+}]$  around the activating sites of a TRPM2 channel, resulting from  $\text{Ca}^{2+}$  ions entering through its pore, is unlikely to be completely dissipated before that channel reopens. This allows extracellular  $\text{Ca}^{2+}$  alone to maintain steady-state TRPM2 activity (McHugh et al., 2003; Starkus et al., 2007). Moreover, it is likely that channels sense some of the  $\text{Ca}^{2+}$  entering through the pores of nearby channels. Thus, in an intact cell, extracellular  $\text{Ca}^{2+}$  provides robust positive feedback to TRPM2 activation. Our results suggest that in living cells that contain as little as a few micromolar ADPR a single puff of  $\text{Ca}^{2+}$  is sufficient to trigger prolonged, self-sustained TRPM2 activity.

We thank Dóra Mayer for oocyte isolation and injection.

L. Csanády is a Bolyai Research Fellow of the Hungarian Academy of Sciences. This work was supported by Országos Tudományos Kutatási Alapprogramok grant F 68143 to L. Csanády.

Edward N. Pugh Jr. served as editor.

Submitted: 21 August 2008

Accepted: 6 January 2009

## REFERENCES

- Beck, A., M. Kolisek, L.A. Bagley, A. Fleig, and R. Penner. 2006. Nicotinic acid adenine dinucleotide phosphate and cyclic ADP-ribose regulate TRPM2 channels in T lymphocytes. *FASEB J.* 20:962–964.
- Buelow, B., Y. Song, and A.M. Scharenberg. 2008. The poly(ADP-ribose) polymerase PARP-1 is required for oxidative stress-induced TRPM2 activation in lymphocytes. *J. Biol. Chem.* 283:24571–24583.
- Chan, K.W., L. Csanády, D. Seto-Young, A.C. Nairn, and D.C. Gadsby. 2000. Severed molecules functionally define the boundaries of the cystic fibrosis transmembrane conductance regulator's  $\text{NH}_2$ -terminal nucleotide binding domain. *J. Gen. Physiol.* 116:163–180.
- Colquhoun, D., and F.J. Sigworth. 1995. The principles of the stochastic interpretation of ion-channel mechanisms. In *Single Channel Recording*. B. Sakmann and E. Neher, editors. Plenum Press, New York. 397–482.
- Csanády, L. 2000. Rapid kinetic analysis of multichannel records by a simultaneous fit to all dwell-time histograms. *Biophys. J.* 78:785–799.
- Csanády, L., and V. Adam-Vizi. 2004. Antagonistic regulation of native  $\text{Ca}^{2+}$ - and ATP-sensitive cation channels in brain capillaries by nucleotides and decavanadate. *J. Gen. Physiol.* 123:743–757.
- Grubisha, O., L.A. Rafty, C.L. Takanishi, X. Xu, L. Tong, A.L. Perraud, A.M. Scharenberg, and J.M. Denu. 2006. Metabolite of SIR2 reaction modulates TRPM2 ion channel. *J. Biol. Chem.* 281:14057–14065.
- Hamill, O.P., A. Marty, E. Neher, B. Sakmann, and F.J. Sigworth. 1981. Improved patch-clamp techniques for high-resolution current recording from cells and cell-free membrane patches. *Pflügers Arch.* 391:85–100.
- Hill, K., N.J. Tigue, R.E. Kelsell, C.D. Benham, S. McNulty, M. Schaefer, and A.D. Randall. 2006. Characterisation of recombinant rat TRPM2 and a TRPM2-like conductance in cultured rat striatal neurones. *Neuropharmacology*. 50:89–97.
- Jackson, M.B. 1986. Kinetics of unliganded acetylcholine receptor channel gating. *Biophys. J.* 49:663–672.
- Kolisek, M., A. Beck, A. Fleig, and R. Penner. 2005. Cyclic ADP-ribose and hydrogen peroxide synergize with ADP-ribose in the activation of TRPM2 channels. *Mol. Cell.* 18:61–69.
- Kuruma, A., and H.C. Hartzell. 2000. Bimodal control of a  $\text{Ca}^{2+}$ -activated  $\text{Cl}^-$  channel by different  $\text{Ca}^{2+}$  signals. *J. Gen. Physiol.* 115:59–80.
- Lange, I., R. Penner, A. Fleig, and A. Beck. 2008. Synergistic regulation of endogenous TRPM2 channels by adenine dinucleotides in primary human neutrophils. *Cell Calcium*. 44:604–615.
- Launay, P., A. Fleig, A.L. Perraud, A.M. Scharenberg, R. Penner, and J.P. Kinet. 2002. TRPM4 is a  $\text{Ca}^{2+}$ -activated nonselective cation channel mediating cell membrane depolarization. *Cell*. 109:397–407.
- Liman, E.R., J. Tytgat, and P. Hess. 1992. Subunit stoichiometry of a mammalian  $\text{K}^+$  channel determined by construction of multicentric cDNAs. *Neuron*. 9:861–871.
- Maruyama, Y., T. Ogura, K. Mio, S. Kiyonaka, K. Kato, Y. Mori, and C. Sato. 2007. Three-dimensional reconstruction using transmission electron microscopy reveals a swollen, bell-shaped structure of transient receptor potential melastatin type 2 cation channel. *J. Biol. Chem.* 282:36961–36970.
- McHugh, D., R. Flemming, S.Z. Xu, A.L. Perraud, and D.J. Beech. 2003. Critical intracellular  $\text{Ca}^{2+}$  dependence of transient receptor potential melastatin 2 (TRPM2) cation channel activation. *J. Biol. Chem.* 278:11002–11006.
- Monod, J., J. Wyman, and J.P. Changeux. 1965. On the nature of allosteric transitions: a plausible model. *J. Mol. Biol.* 12:88–118.
- Nagamine, K., J. Kudoh, S. Minoshima, K. Kawasaki, S. Asakawa, F. Ito, and N. Shimizu. 1998. Molecular cloning of a novel putative  $\text{Ca}^{2+}$  channel protein (TRPC7) highly expressed in brain. *Genomics*. 54:124–131.
- Nilius, B., G. Owsianik, T. Voets, and J.A. Peters. 2007. Transient receptor potential cation channels in disease. *Physiol. Rev.* 87:165–217.
- Pérez, G.J., A.D. Bonev, and M.T. Nelson. 2001. Micromolar  $\text{Ca}^{2+}$  from sparks activates  $\text{Ca}^{2+}$ -sensitive  $\text{K}^+$  channels in rat cerebral artery smooth muscle. *Am. J. Physiol. Cell Physiol.* 281:C1769–C1775.
- Perraud, A.L., A. Fleig, C.A. Dunn, L.A. Bagley, P. Launay, C. Schmitz, A.J. Stokes, Q. Zhu, M.J. Bessman, R. Penner, et al. 2001. ADP-ribose gating of the calcium-permeable LTRPC2 channel revealed by Nudix motif homology. *Nature*. 411:595–599.
- Perraud, A.L., B. Shen, C.A. Dunn, K. Rippe, M.K. Smith, M.J. Bessman, B.L. Stoddard, and A.M. Scharenberg. 2003. NUDT9, a member of the Nudix hydrolase family, is an evolutionarily conserved mitochondrial ADP-ribose pyrophosphatase. *J. Biol. Chem.* 278:1794–1801.
- Perraud, A.L., C.L. Takanishi, B. Shen, S. Kang, M.K. Smith, C. Schmitz, H.M. Knowles, D. Ferraris, W. Li, J. Zhang, et al. 2005. Accumulation of free ADP-ribose from mitochondria mediates oxidative stress-induced gating of TRPM2 cation channels. *J. Biol. Chem.* 280:6138–6148.
- Qu, Z., and H.C. Hartzell. 2000. Anion permeation in  $\text{Ca}^{2+}$ -activated  $\text{Cl}^-$  channels. *J. Gen. Physiol.* 116:825–844.
- Rohacs, T., C.M. Lopes, I. Michailidis, and D.E. Logothetis. 2005.  $\text{PI}(4,5)\text{P}_2$  regulates the activation and desensitization of TRPM8 channels through the TRP domain. *Nat. Neurosci.* 8:626–634.
- Rothberg, B.S., and K.L. Magleby. 1999. Gating kinetics of single large-conductance  $\text{Ca}^{2+}$ -activated  $\text{K}^+$  channels in high  $\text{Ca}^{2+}$  suggest a two-tiered allosteric gating mechanism. *J. Gen. Physiol.* 114:93–124.
- Sakmann, B., and E. Neher, editors. 1995. *Single Channel Recording*. Second edition. Plenum Press, New York. 700 pp.

- Sano, Y., K. Inamura, A. Miyake, S. Mochizuki, H. Yokoi, H. Matsushime, and K. Furuichi. 2001. Immunocyte Ca<sup>2+</sup> influx system mediated by LTRPC2. *Science*. 293:1327–1330.
- Starkus, J., A. Beck, A. Fleig, and R. Penner. 2007. Regulation of TRPM2 by extra- and intracellular calcium. *J. Gen. Physiol.* 130:427–440.
- Tong, Q., W. Zhang, K. Conrad, K. Mostoller, J.Y. Cheung, B.Z. Peterson, and B.A. Miller. 2006. Regulation of the transient receptor potential channel TRPM2 by the Ca<sup>2+</sup> sensor calmodulin. *J. Biol. Chem.* 281:9076–9085.
- Ullrich, N.D., T. Voets, J. Prenen, R. Vennekens, K. Talavera, G. Droogmans, and B. Nilius. 2005. Comparison of functional properties of the Ca<sup>2+</sup>-activated cation channels TRPM4 and TRPM5 from mice. *Cell Calcium*. 37:267–278.
- Wehage, E., J. Eisefeld, I. Heiner, E. Jungling, C. Zitt, and A. Luckhoff. 2002. Activation of the cation channel long transient receptor potential channel 2 (LTRPC2) by hydrogen peroxide. A splice variant reveals a mode of activation independent of ADP-ribose. *J. Biol. Chem.* 277:23150–23156.